A polarization insensitive and wide-angle dual-band nearly perfect absorber in the infrared regime

2012 J. Opt. 14 085102

(http://iopscience.iop.org/2040-8986/14/8/085102)

IOP Publishing Journal of Optics
J. Opt. **14** (2012) 085102 (5pp) doi:10.1088/2040-8978/14/8/085102

A polarization insensitive and wide-angle dual-band nearly perfect absorber in the infrared regime

Hua Cheng[1], Shuqi Chen[1], Haifang Yang[2], Junjie Li[2], Xin An[1], Changzhi Gu[2] and Jianguo Tian[1]

[1] The Key Laboratory of Weak Light Nonlinear Photonics, Ministry of Education, School of Physics and Teda Applied Physics School, Nankai University, Tianjin 300457, People's Republic of China
[2] Beijing National Laboratory for Condensed Matter Physics, Institute of Physics, Chinese Academy of Sciences, PO Box 603, Beijing 100190, People's Republic of China

E-mail: schen@nankai.edu.cn and jjtian@nankai.edu.cn

Received 10 April 2012, accepted for publication 2 July 2012
Published 13 July 2012
Online at stacks.iop.org/JOpt/14/085102

Abstract
We report the design, characterization, and experimental demonstration of an infrared dual-band metamaterial absorber composed of simple periodically patterned structures. Experimental results show that two distinct absorption peaks of 74% and 96% are obtained, which are in reasonable agreement with the simulations. We demonstrate two absorption resonances that are derived from the mixture of magnetic and electric plasmon resonances. The dual-band absorber is polarization insensitive and the absorption peaks remain high with large angles of incidence for both transverse electric and transverse magnetic polarizations, which provide more efficient absorptions for nonpolarized or oblique incident beams.

Keywords: metamaterial absorber, dual-band, polarization insensitive, wide angle

(Some figures may appear in colour only in the online journal)

1. Introduction

The near perfect absorption component is one of the fundamental building blocks for photodetectors [1], microbolometers [2], thermal imagers [3], and absorbers used in thermal photovoltaic solar energy conversion [4]. Metamaterial based absorbers may have promising potential in these areas due to their unique ability to achieve unity absorption with high efficiency [5]. Since the first microwave metamaterial absorber (MA) was demonstrated, many efforts have focused on extending highly absorbing metamaterials to smaller wavelengths [6–9]. As a result of different applications, the research interest in MAs was extended from a single narrow band to broadband [10, 11] and dual bands or multibands [12–15]. Dual-band MAs have attracted considerable interest due to their potential applications in the spectroscopic detection and phase imaging of prohibited drugs and explosive materials, that show distinct absorptions or 'fingerprints' at multifrequencies [16]. Wen *et al* [12] and Tao *et al* [13] proposed a design for dual-band MAs in the terahertz regime. However, both of these dual-band MAs depend strongly on the polarization of the incident wave as well as the angle of incidence. They work well only for one polarization at normal incidence and the absorption drops rapidly for off-normal-incidence cases, which limits the device applications of these absorbing structures. Recently, Ma *et al* [14] proposed a polarization insensitive and wide-angle dual-band MA in the terahertz regime. However, its resonant mechanisms are based only on magnetic polaritons and the absorptions are in the terahertz regime; the fabrication of such devices in this regime is far simpler than that of devices in the infrared and optical frequencies. Liu *et al* [17] and Jiang *et al* [18] also proposed dual-band MAs in the mid-infrared regime. However, the two resonant absorptions in [17] and the short-wavelength resonant absorption in [18] are attributed to the nearly pure magnetic response of the structure.

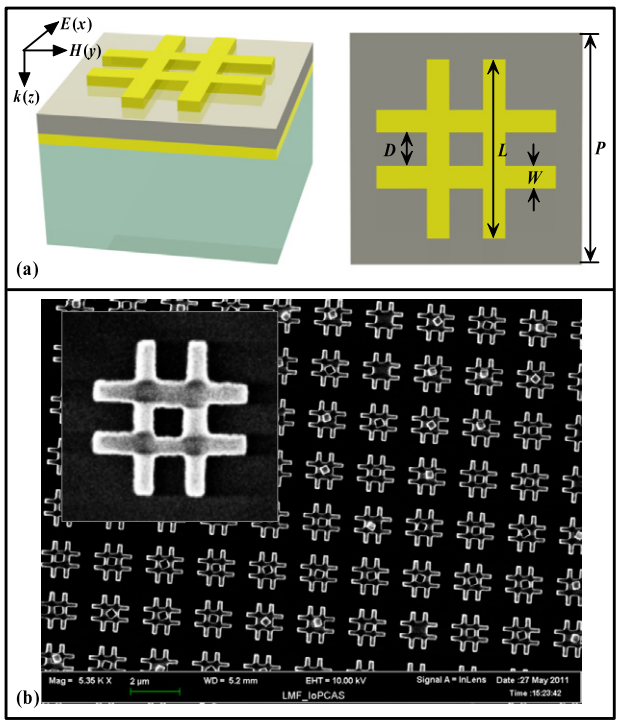

Figure 1. (a) Schematic diagram of the infrared dual-band MA design and the incident light polarization configuration. The geometry parameters are as follows: unit cell length $P = 2.1$ μm; bar length and width $L = 1.5$ μm and $W = 0.2$ μm; interspace between two bars $D = 0.3$ μm. (b) Top-view scanning electron micrographs of the dual-band MA. Inset: enlarged view.

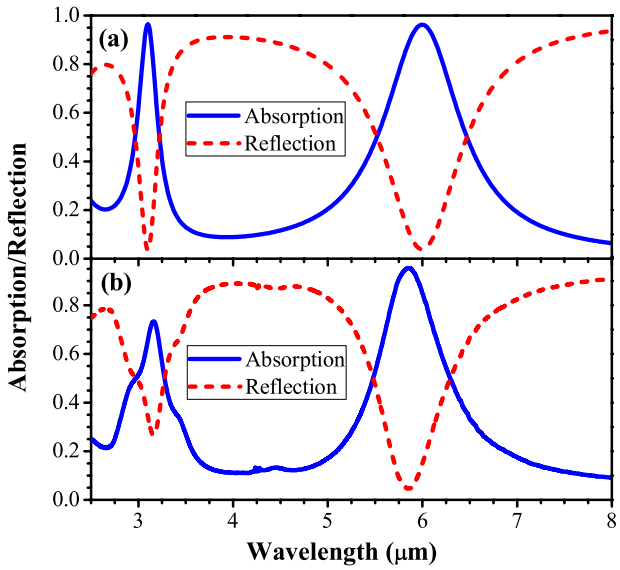

Figure 2. (a) Simulated and (b) experimental reflection (red dashed line) and absorption (blue solid line) spectra of the infrared dual-band absorber.

In this paper, we present the design, characterization, and experimental demonstration of a dual-band MA in the infrared regime. The structure has a single patterned top layer with #-shaped wires, which is simple and easy to fabricate. The two absorption resonances of the dual-band MA are induced by the mixture of electric and magnetic plasmon resonances, and are the fundamental order resonance (at 6 μm) and the higher order resonance (at 3.1 μm) of the #-shaped gold wires. The experimental peak absorptions of our fabricated infrared dual-band MA reach 74% at 3.15 μm and 96% at 5.86 μm. In addition, the absorption resonances are polarization insensitive due to the symmetry of the unit cell, and absorptions remain high even at large angles of incidence for both TE and TM polarizations. These are useful for applications as absorbing elements, since absorption can be maximized for wide-angle and arbitrarily polarized or incoherent incident light.

2. The structure design and simulations

The designed and fabricated dual-band MA is shown in figure 1, with its geometrical parameters described in the caption. It contains two metallic elements: an array of 100 nm thick gold structures and a 100 nm thick gold board, which are separated by 185 nm thick Al_2O_3 with the dielectric constant and loss tangent of 2.28 and 0.04 [3]. All three layers are fabricated on silicon substrate with permittivity of 11.7. The optimized structure was achieved by using the finite element method based commercial software COMSOL Multiphysics 3.4 [19]. The optical constants of bulk gold in the infrared spectral regime are described by using the Drude model with the plasma frequency $\omega_p = 1.37 \times 10^{16}$ s^{-1} and the damping constant $\omega_c = 4.08 \times 10^{13}$ s^{-1} [20].

For numerical simulations, we only consider a single unit cell with periodic boundary conditions in all $\hat{y}\hat{z}$ planes and $\hat{x}\hat{z}$ planes, and waveguide port boundary conditions on the other boundaries, as shown on the left in figure 1(a). The reflection $R(\omega)$ and transmission of $T(\omega)$ are obtained from the S-parameters as $R(\omega) = |S_{11}(\omega)|^2$ and $T(\omega) = |S_{21}(\omega)|^2$, where the S_{11} and S_{21} are the complex reflection and transmission, respectively. The reflectance is obtained by integrating the entire scattered field above the sample, which includes all the diffracted orders. Thus, the absorption can be calculated according to $A(\omega) = 1 - R(\omega) - T(\omega)$. Assuming an incident beam normal to the upper face of the MA (see in figure 1), the wavelength dependence of reflection and absorption are calculated in figure 2(a). The transmission is effectively zero across the entire infrared wavelength range, because the metallic ground plane is thicker than the penetration depth of light in the infrared regime. Two distinct resonances occur at 3.1 μm and 6.0 μm in the reflection spectrum, respectively, thus yielding two maxima in the absorption. The absorption peaks at 3.1 μm and 6.0 μm are both 96%, and the absorption bandwidths, defined as the full widths at half-maximum, are 0.27 μm and 0.99 μm for the short-wavelength and long-wavelength peaks, respectively.

3. Experiments

In our experiments, the substrate consists of a 3 mm thickness of silicon board. Ti(5 nm)/Au(100 nm) was deposited on the substrate by e-beam deposition. This was followed by e-beam deposition of a 185 nm thickness layer of Al_2O_3. The

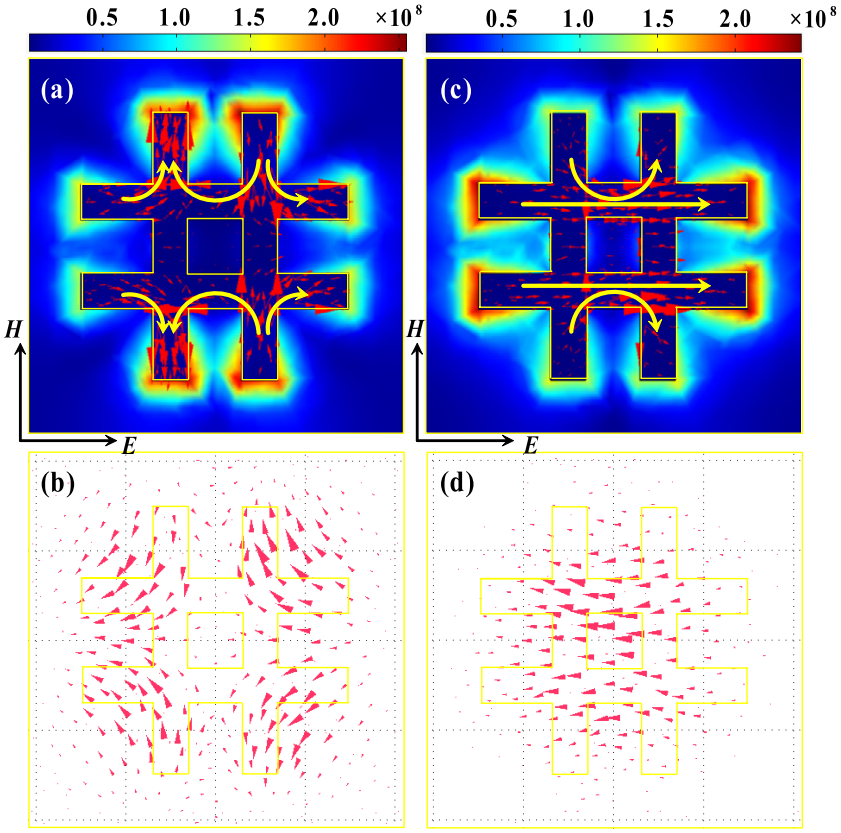

Figure 3. Distribution of the induced surface current density of the #-shaped resonator ((a) and (c)) and the ground gold plane ((b) and (d)) for short- and long-wavelength absorption peaks. The color maps represent the amplitudes of the electric field distributions at the short- and long-wavelength absorption peaks.

top patterned layer was defined by e-beam lithography. Then Cr(5 nm)/Au(100 nm) was evaporated, and the pattern transfer was completed by metal liftoff. Figure 1(b) shows a scanning electron microscopy (SEM) image of the fabricated infrared dual-band MA. A Bruker VERTEX 70 Fourier-transform IR spectrometer was used to measure the reflection spectrum. The reflection of the sample was recorded by averaging measured data over 64 measurements in order to improve the signal-to-noise ratio. For reflection measurements, the incident unpolarized light was inclined at an angle of about 30° with respect to the normal on the sample surface. Before measuring the MA sample, the reflection was calibrated with a gold plate. In the measurements, only the zero diffracted order of reflection is detected, since the higher diffracted orders have little influence on the measured reflectance with an angle of incidence of 30°.

The experimentally obtained absorption and reflection spectra are shown in figure 2(b). Two resonant absorption peaks of 74% at 3.15 μm and 96% at 5.86 μm are obtained, which are in reasonable agreement with the simulations, though the absorption peaks are lower than expected, partly due to inclined incidence in the experiment. The angle of incidence has more effect on the amplitude of the short-wavelength absorption peak than that of the long-wavelength absorption peak. There are noticeable wavelength shifts of 0.05 μm at the low resonant wavelength and 0.14 μm at the high resonant wavelength between the experimental and simulation results, which are mainly due to the inaccuracies of the fabrication, i.e., in bar length, bar width, and interspaces between the two bars. The off-resonance absorption (∼0.2) is in quite good agreement with the simulation.

4. Discussion

To get insight into the nature of the dual-band absorption, we calculated the surface current distributions in the #-shaped gold resonator (in figures 3(a) and (c)) and the lower ground gold plane (in figures 3(b) and (d)) by exciting with photon energy corresponding to the resonances at 3.1 μm (in figures 3(a) and (b)) and at 6.0 μm (in figures 3(c) and (d)). Furthermore, the moduli of the electric field near the surface of the #-shaped gold wire for the resonances at 3.1 and 6.0 μm are also demonstrated in figures 3(a) and (b). The indicative yellow arrows are added to mark the foremost direction of the surface current in figures 3(a) and (c). Both the electric and the magnetic plasmon resonances contribute to the resonance at 3.1 μm. Surface currents flowing around the upper and lower gaps of the #-shaped gold resonator are attributable to magnetic plasmon resonances, which can be characterized as *LC*-resonances, as the arms serve like an inductance *L* and the gap between the two arms provides the capacitance *C*. The electric field is coupled into the upper and lower gaps near the vertices of the arms of the #-shaped gold wire, as the *LC*-resonances. The charges also accumulate at the corners

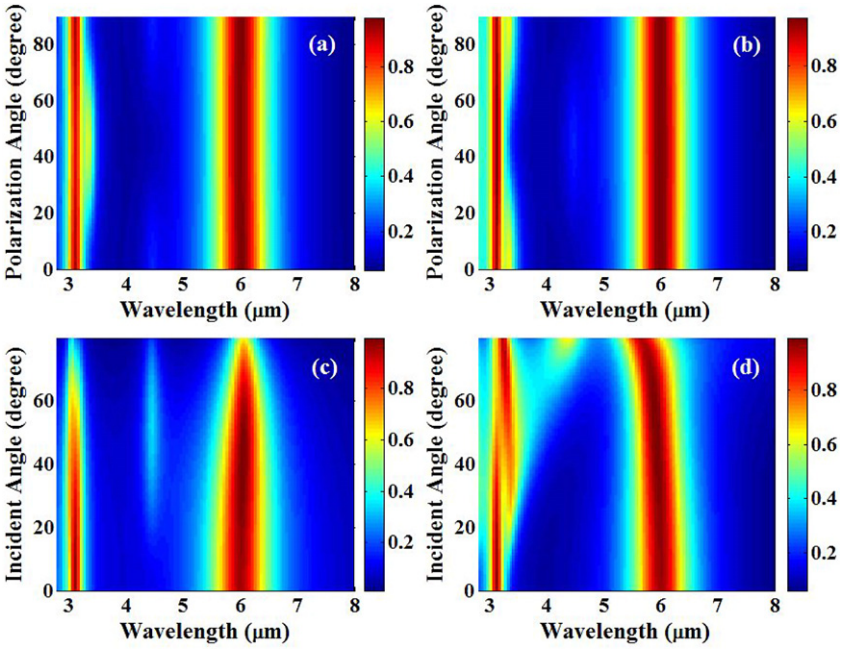

Figure 4. Simulated absorption spectra as a function of wavelength and the polarization angle for (a) TE polarization and (b) TM polarization. Simulated absorption spectra as a function of wavelength and the angle of incidence for (c) TE polarization and (d) TM polarization.

of the #-shaped gold wire owing to the electrical plasmon resonances. The surface currents flowing around the outer arms also exhibit this tendency. For the resonance at 6.0 μm, the electric fields are coupled into the upper and lower gaps near the vertices of the arms on account of the *LC*-resonances (see in figure 3(c)). There also exist strong electric dipole resonances arising from charge accumulation at the left and right corners, as indicated by the straight yellow arrows in figure 3(c). For both resonances, there exist antiparallel currents between the #-shaped resonator and the ground plane (see in figures 3(c) and (d)). Thus magnetic responses associated with circulating displacement currents between the #-shaped resonator and the ground plane lead to magnetic field accumulation in the dielectric spacer. It should be noted that the major difference between the findings of [17, 18] and our results is in the mechanism of the resonant absorption. The short-wavelength resonant absorption in [18] is attributable to the nearly pure magnetic resonances of differently oriented H-structures. However, the two resonant absorptions of our proposed dual-band MA are induced by the mixture of electric and magnetic plasmon resonances in the same #-resonator, which can be regarded as the fundamental order resonance (at about 6.0 μm) and the higher order resonance (at about 3.1 μm) of the #-shaped gold wires.

The polarization insensitive performance is important in practical applications. In some cases, most of the possible light needs to be absorbed, and it may contain arbitrarily polarized components. To demonstrate the polarization insensitive behavior, we plot the simulated absorption spectra as a function of polarization angle for both TE (figure 4(a)) and TM (figure 4(b)) configurations in figure 4, where the angle of incidence is fixed at 20°. The polarization angle is defined as the angle between the polarized direction and the x axis of the coordinate, which is equivalent to rotating the sample while fixing the polarized direction. The angle of incidence is defined as the angle between the wavevector and the z axis of the coordinate. It is clearly seen that the absorption spectra of the proposed dual-band MA are polarization insensitive. Our designed dual-band structure can also work as a near perfect MA over a wide range of angles of incidence. Figures 4(c) and (d) give the angular dispersion of the absorption spectra for both TE and TM configurations, where the azimuthal angle is fixed at 0°. For the TE polarization, the peak absorptions of 96% are obtained at normal incidence for the resonances at 3.1 and 6.0 μm. The absorption will decrease with increasing of angle of incidence. The absorption of the resonance at 3.1 μm can still remain as high as 82% at the angle of incidence of 40°. Beyond this, there is a monotonic decrease in the absorption as the incident magnetic field can no longer efficiently drive circulating currents between the two metallic layers. The absorption of the resonance at 6.0 μm remains about 0.83 at the angle of incidence of 70°, and beyond this it decreases quickly. For the TM polarization, the absorption is nearly independent of the angle of incidence. For the angle of incidence of 80°, the short-wavelength absorption peak remains 92%, and the long-wavelength absorption peak remains 93%. When the angles of incidence change from 0° to 80°, the short- and long-wavelength resonances for the TM polarization have a redshift of 0.15 μm and a blueshift of 0.35 μm, respectively. These results reveal that the proposed dual-band MA operates quite well both for TE and for TM radiation over a wide range of angles of incidence. The aforementioned advantages make it a good candidate for use in the design of high performance absorbers used in explosives detection, bolometers, thermal detectors, spectroscopic imaging, etc.

5. Conclusions

In conclusion, we have designed and fabricated an infrared dual-band MA composed of simple periodically patterned #-shaped metal structures, continuous metal film, a dielectric spacer and a dielectric substrate. The fabricated samples were characterized by measuring the reflection spectra. Two distinct resonant absorption peaks with 74% and 96% are achieved experimentally, which is in reasonable agreement with the simulations. The dual-band MA is polarization insensitive and both of the absorption bands remain high even with large angles of incidence for both TE and TM polarizations. These are features useful in some respects, since absorption can be maximized for wide-angle and arbitrarily polarized or incoherent incident light.

Acknowledgments

This research was supported by the Chinese National Key Basic Research Special Fund (Grant No. 2011CB922003), the National Natural Science Foundation of China (Grant Nos 61008002 and 91023041), the National Basic Research Program of China (Grant No. 2009CB930502), the Specialized Research Fund for the Doctoral Program of Higher Education (Grant No. 20100031120005), the Fundamental Research Funds for the Central Universities (Grant Nos 65012351 and 65010801), and the 111 project (grant B07013).

References

[1] Hayden O, Agarwal R and Lieber C M 2006 *Nature Mater.* **5** 352–6
[2] Richards P L 1994 *J. Appl. Phys.* **76** 1–24
[3] Liu X, Starr T, Starr A F and Padilla W J 2010 *Phys. Rev. Lett.* **104** 207403
[4] Tian B, Zheng X L, Kempa T J, Fang Y, Yu N F, Yu G H, Huang J L and Lieber C M 2007 *Nature* **449** 885–9
[5] Landy N I, Sajuyigbe S, Mock J J, Smith D R and Padilla W J 2008 *Phys. Rev. Lett.* **100** 207402
[6] Tao H, Bingham C M, Strikwerda A C, Pilon D, Shrekenhamer D, Landy N I, Fan K, Zhang X, Padilla W J and Averitt R D 2008 *Phys. Rev.* B **78** 241103
[7] Landy N I, Bingham C M, Tyler T, Jokerst N, Smith D R and Padilla W J 2009 *Phys. Rev.* B **79** 125104
[8] Hao J, Wang J, Liu X, Padilla W J, Zhou L and Qiu M 2010 *Appl. Phys. Lett.* **96** 251104
[9] Liu N, Mesch M, Weiss T, Hentschel M and Giessen H 2010 *Nano Lett.* **10** 2342–8
[10] Grant J, Ma Y, Saha S, Khalid A and Cumming D R S 2011 *Opt. Lett.* **36** 3476–8
[11] Chen S, Cheng H, Yang H, Li J, Duan X, Gu C and Tian J 2011 *Appl. Phys. Lett.* **99** 253104
[12] Wen Q, Zhang H, Xie Y, Yang Q and Liu Y 2009 *Appl. Phys. Lett.* **95** 241111
[13] Tao H, Bingham C M, Pilon D, Fan K, Strikwerda A C, Shrekenhamer D, Padilla W J, Zhang X and Averitt R D 2010 *J. Phys. D: Appl. Phys.* **43** 225102
[14] Ma Y, Chen Q, Grant J, Saha S C, Khalid A and Cumming D R S 2011 *Opt. Lett.* **36** 945–7
[15] Shen X, Cui T J, Zhao J, Ma H F, Jiang W X and Li H 2011 *Opt. Express* **19** 9401–7
[16] Zhang L L, Zhong H, Deng C, Zhang C L and Zhao Y J 2008 *Appl. Phys. Lett.* **92** 091117
[17] Liu X, Tyler T, Starr T, Starr A F, Jokerst N M and Padilla W J 2011 *Phys. Rev. Lett.* **107** 045901
[18] Jiang Z H, Yun S, Toor F, Werner D H and Mayer T S 2011 *ACS Nano* **5** 4641–7
[19] COMSOL A B 2008 *COMSOL Multiphysics User's Guide, Version 3.4* Burlington, MA
[20] Ordal M A, Long L L, Bell R J, Bell S E, Bell R R, Alexander R W and Ward C A 1983 *Appl. Opt.* **22** 1099–119